nature photonics

Article

https://doi.org/10.1038/s41566-023-01351-5

Bright and stable near-infrared lead-free perovskite light-emitting diodes

Received: 5 April 2023

Accepted: 17 November 2023

Published online: 5 January 2024

Check for updates

Fanglong Yuan[1,2], Giulia Folpini[3], Tianjun Liu[1], Utkarsh Singh[1], Antonella Treglia[3,4], Jia Wei Melvin Lim[5], Johan Klarbring[1], Sergei I. Simak[1,6], Igor A. Abrikosov[1], Tze Chien Sum[5], Annamaria Petrozza[3] & Feng Gao[1]

Long-wavelength near-infrared light-emitting diodes (NIR LEDs) with peak emission wavelengths beyond 900 nm are of critical importance for various applications including night vision, biomedical imaging, sensing and optical communications. However, the low radiance and poor operational stability of state-of-the-art long-wavelength NIR LEDs based on soft materials remain the most critical factors limiting their practical applications. Here we develop NIR LEDs emitting beyond 900 nm with improved performance through the rational manipulation of p doping in all-inorganic tin perovskites ($CsSnI_3$) by retarding and controlling the crystallization process of perovskite precursors in tin-rich conditions. The resulting NIR LEDs exhibit a peak emission wavelength at 948 nm, high radiance of 226 W sr^{-1} m^{-2} and long operational half-lifetime of 39.5 h at a high constant current density of 100 mA cm^{-2}. Our demonstration of efficient and stable NIR LEDs operating at high current densities may also open up new opportunities towards electrically pumped lasers.

Near-infrared (NIR) light-emitting diodes (LEDs) are of great interest for diverse applications including night vision, biomedical imaging, sensing and optical communications[1–4]. Present-day NIR emitters primarily rely on III–V epitaxial hard inorganic semiconductors (such as GaAs and AlInGaAs)[5,6]. However, the harsh and complicated high-temperature processing increases their cost and limits their integration in multifunctional photonic platforms. Therefore, great efforts have been made to develop alternative soft NIR emitters that can overcome these drawbacks. Although substantial strides have been made for short-wavelength NIR LEDs with emission peak below 900 nm (refs. 7–9), long-wavelength NIR LEDs over 900 nm based on organic semiconductors and colloidal quantum dots (QDs) still face primary challenges of low radiance and poor operational stability (Table 1), limiting their practical applications[10–14].

Metal halide perovskites are promising candidates for LEDs due to their excellent optical and electrical properties[15–19]. Tin-based halide perovskites (THPs), especially all-inorganic black orthorhombic (γ)-$CsSnI_3$, are promising for use in NIR LEDs due to their low bandgap (~1.3 eV), high hole mobilities and excellent intrinsic inorganic structural stability[20–32]. However, the easy oxidation of Sn^{2+} to Sn^{4+} usually results in p doping with high background hole densities, leading to strong non-radiative recombinations[33,34].

In spite of the strong p doping in THPs, we notice that doping is not necessarily detrimental towards device performance, as long as the doping can be controlled. For example, electronic doping in conventional III–V-group inorganic semiconductors is one of the most powerful tools in established technologies, allowing for the fine-tuning of their functionalities and creating the base for modern microelectronics. It has been demonstrated that intentional electronic doping in semiconductors could boost emission properties as a result of the radiative recombinations of doped holes with free electrons[35–38]. Inspired by the development

[1]Department of Physics, Chemistry, and Biology (IFM), Linköping University, Linköping, Sweden. [2]Key Laboratory of Theoretical and Computational Photochemistry of Ministry of Education, College of Chemistry, Beijing Normal University, Beijing, China. [3]Center for Nano Science and Technology@PoliMi, Istituto Italiano di Tecnologia, Milan, Italy. [4]Physics Department, Politecnico di Milano, Milan, Italy. [5]Division of Physics and Applied Physics, School of Physical and Mathematical Sciences, Nanyang Technological University, Singapore, Singapore. [6]Department of Physics and Astronomy, Uppsala University, Uppsala, Sweden. e-mail: feng.gao@liu.se

https://doi.org/10.1038/s41566-023-01351-5

Table 1 | Key performance parameters of state-of-the-art NIR LEDs (>900 nm) based on different kinds of material

Materials category and examples		Emission peak (nm)	FWHM (nm)	Radiance ($W sr^{-1} m^{-2}$)	Stability (T_{50})	Ref.
Organic molecules	Pt(II) complexes	930	>200	41.6	NA	10
Pb-based QDs	PbS/PbS QD/ZnO	1,400	~200	9	NA	11
	PbS QD/perovskite	980	~150	7.4	~1 h (10 mA cm^{-2})	13
Ag-based QDs	$Ag_2S@SiO_2$ QDs	1,397	~75	83.9	NA	14
Lead–tin halides	FPMAI-$MAPb_{0.6}Sn_{0.4}I_3$	917	~100	2.7	~3 min (5 mA cm^{-2})	20
Inorganic tin halides	$CsSnI_3$	948	71	226	39.5 h (100 mA cm^{-2})	This work

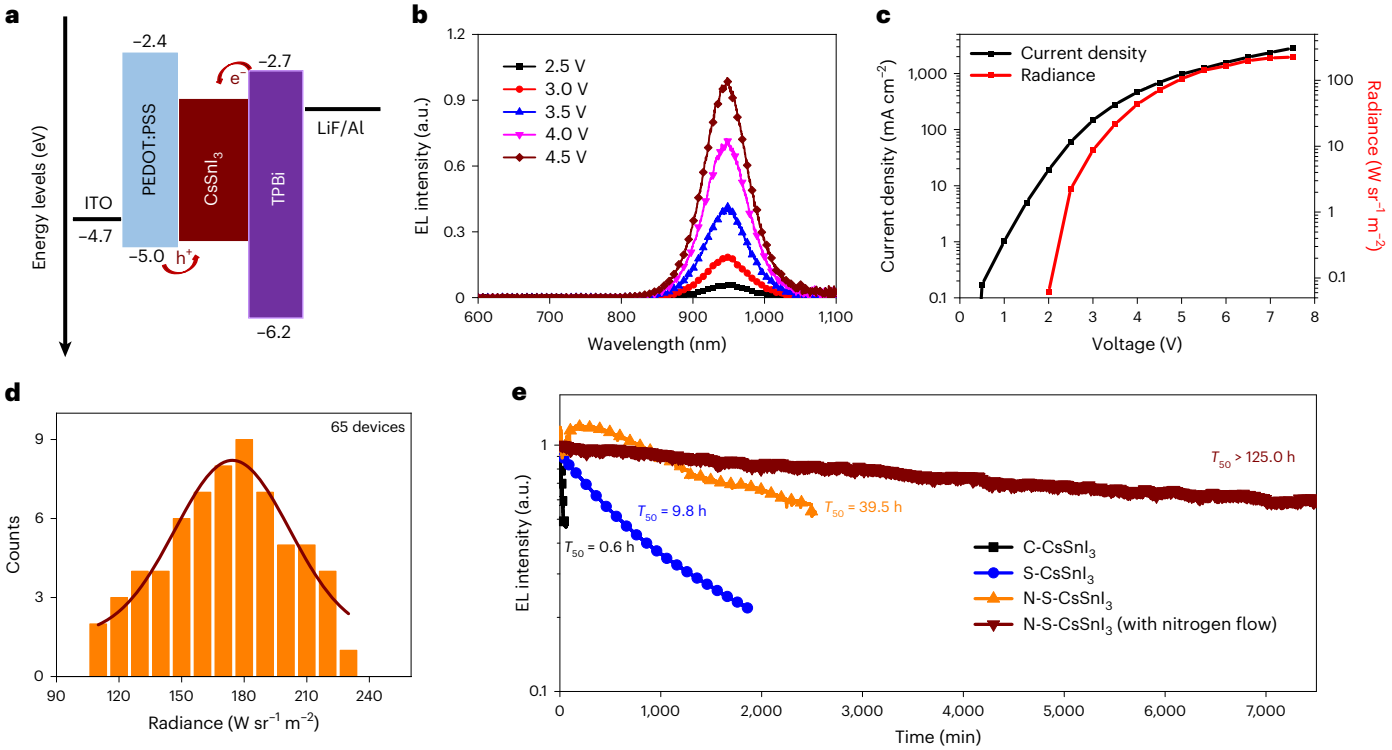

Fig. 1 | LED structure and performance. a, Energy-level diagram. **b**, The EL spectra at different operating voltages. **c**,**d**, Current density–voltage–radiance (**c**) and histograms of maximum radiance (**d**) of N-S-$CsSnI_3$ LEDs. **e**, Operational stability of LEDs prepared under different conditions at a constant current density of 100 mA cm^{-2}. The stability of N-S-$CsSnI_3$ LEDs are measured with (dark red line) and without (orange line) a nitrogen flow for comparison.

of electronic doping in inorganic semiconductors for improved LED performance, we, thus, believe that the intrinsic p-doping characteristic of THPs could be beneficial for achieving high-performance NIR LEDs through elaborately controlling the hole-doping and trap densities.

Here we report long-wavelength NIR LEDs peaking at 948 nm with high radiance and long operational stability based on $CsSnI_3$, achieved by simultaneously exploiting the beneficial effect of intrinsic p doping in THPs and reducing the carrier trap density. A facile yet effective strategy is developed to control the intrinsic p-doping density and reduce the trap density by controlling the crystallization process of $CsSnI_3$ precursors in tin-rich conditions, leading to improved radiative efficiency and stability. Leveraging these benefits, we demonstrate NIR LEDs with a high radiance of 226 W sr^{-1} m^{-2} and an operational half-lifetime of 39.5 h at a high constant current density of 100 mA cm^{-2}, both significantly exceeding the previously reported soft-materials-based NIR LEDs with emission peaks over 900 nm.

Device structure and performance

We fabricate $CsSnI_3$-based NIR LEDs with the following device architecture: indium tin oxide (ITO) glass substrate anode, a poly(3,4-ethylenedioxythiophene):poly(styrene-sulfonate) (PEDOT:PSS) hole injection layer, an active $CsSnI_3$ emission layer, a 1,3,5-tris (*N*-phenylbenzimidazol-2-yl) benzene (TPBi) electron transport layer and a LiF/Al cathode (Fig. 1a). $CsSnI_3$ films are prepared by spin coating from SnI_2 and CsI precursors with additives of N-phenylthiourea (NPTU) and SnF_2 (denoted as N-S-$CsSnI_3$). SnF_2 has been widely used in THP-based solar cells, providing a tin-rich condition to reduce the intrinsic hole-doping density mainly due to Sn vacancies. NPTU helps to retard the crystallization process, which—as we show later—further manipulates the intrinsic p-doping density as well as reduces the carrier trap density. Control $CsSnI_3$ films treated without additives (C-$CsSnI_3$) and with SnF_2 (S-$CsSnI_3$) are also prepared for comparison. A cross-sectional scanning electron microscopy (SEM) image (Supplementary Fig. 1) of the device shows the formation of discrete submicrometre-structured perovskite crystals in the emission layer. The thickness of the perovskite film was determined to be around 40–50 nm. The emission peak of the electroluminescence (EL) spectra of N-S-$CsSnI_3$ LEDs is centred at ~948 nm, which is redshifted compared with that of ~920 and ~942 nm for C- and S-$CsSnI_3$ LEDs (Supplementary Fig. 2). In addition, a reduced full-width at half-maximum (FWHM) of

https://doi.org/10.1038/s41566-023-01351-5

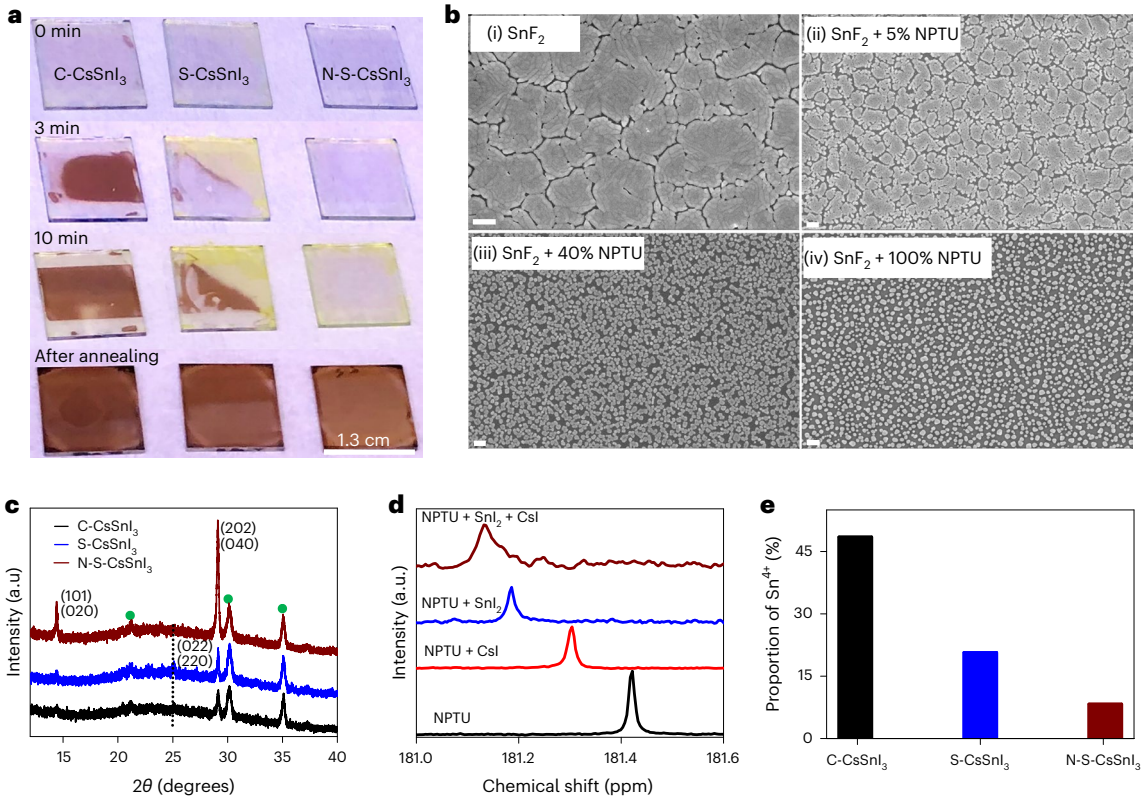

Fig. 2 | Preparation, morphology and structural characterizations of $CsSnI_3$ films. a, Photographs of $CsSnI_3$ films prepared under different conditions before and after annealing, where 0, 3 and 10 min indicate the films before annealing. **b**, SEM images of S-$CsSnI_3$ (i), N(5%)-S-$CsSnI_3$ (ii), N(40%)-S-$CsSnI_3$ (iii) and N(100%)-S-$CsSnI_3$ (iv) films. Scale bars, 1 µm. **c**, XRD spectra of $CsSnI_3$ films. The diffraction peaks from the ITO substrate are marked as green cycles. **d**, ^{13}C NMR spectra of NPTU, NPTU + CsI, NPTU + SnI_2 and NPTU + CsI + SnI_2 in a DMSO-d_6 solution. **e**, Proportion of Sn^{4+} of $CsSnI_3$ films prepared under different conditions.

71 nm is obtained for N-S-$CsSnI_3$ LEDs, much smaller than 135 and 81 nm shown by C- and S-$CsSnI_3$ LEDs, respectively. We also observe a negligible shift in the EL spectra under different operating voltages (Fig. 1b and Supplementary Fig. 3), demonstrating good EL spectral stability.

The N-S-$CsSnI_3$ LEDs (Fig. 1c and Supplementary Fig. 4) can operate at a high current density of over 2,800 mA cm^{-2}, and show a corresponding maximum radiance of 226 W sr^{-1} m^{-2}, which is much larger than that of 14 and 103 W sr^{-1} m^{-2} for C- and S-$CsSnI_3$ LEDs (Supplementary Fig. 5, 6). The radiance is also much higher than that of other long-wavelength NIR LEDs with emission peaks over 900 nm, including noble-metal Pt(II)-based organic materials, PbS QDs, Ag_2S QDs and mixed Pb–Sn halide perovskites[10–14,20]. In addition, the N-S-$CsSnI_3$ LEDs show a low efficiency roll-off, with the maximum external quantum efficiency of ~2.63% at a high radiance of 142 W sr^{-1} m^{-2} (Supplementary Fig. 4). The maximum radiance and peak external quantum efficiency histograms of N-S-$CsSnI_3$ LEDs (Fig. 1d and Supplementary Fig. 7) show good reproducibility, demonstrating the effectiveness of the NPTU/SnF_2 incorporation strategy.

Another challenge for THPs is their poor stability, which hinders their practical applications. Notably, N-S-$CsSnI_3$ LEDs exhibit a particularly long operational stability with a half-lifetime (T_{50}) of 39.5 h at a constant current density of 100 mA cm^{-2}, greatly improved compared with C-$CsSnI_3$ LEDs (0.6 h) and S-$CsSnI_3$ LEDs (9.8 h) (Fig. 1e). The T_{50} value for N-S-$CsSnI_3$ LEDs represents the record stability for NIR LEDs with an emission peak of over 900 nm, significantly longer than that of 3 min to 1 h for other NIR LEDs operating at a much smaller constant current density of around 10 mA cm^{-2} (Table 1)[13,20]. This value for N-S-$CsSnI_3$ LEDs can be extended to 125 h when measured under a constant nitrogen flow, indicating that strategies on thermal management would be helpful to further improve the device stability.

Controlled growth of $CsSnI_3$ films

To understand the underlying reasons for improved device performance after the incorporation of NPTU/SnF_2, we perform a range of experiments to investigate the film formation processes. The controlled and retarded crystallization process of $CsSnI_3$ is clearly revealed (Fig. 2a and Supplementary Fig. 8). The colour of C-$CsSnI_3$ quickly changes from light yellow to inhomogeneous dark brown within 10 min after spin coating (without annealing), indicating the fast and uncontrollable crystallization process. This crystallization process is slowed down in S-$CsSnI_3$ and further retarded in N-S-$CsSnI_3$, which changes from colourless to yellow with high transparency within 10 min after spin coating. These results demonstrate that the combination of SnF_2 and NPTU could effectively retard the nucleation and control the crystallization process, leading to the formation of high-quality crystals. After annealing, the N-S-$CsSnI_3$ films show a homogeneous dark brown colour across the entire film. The effect of additives on crystallization is also evidenced from the SEM images (Fig. 2b and Supplementary Fig. 9), where increasing the amount of NPTU leads to a decrease in the areal density of the crystals. Compared with the continuous film, the discontinuous morphology with isolated perovskite grains in the N-S-$CsSnI_3$ films could boost the outcoupling efficiency of the devices, as demonstrated in $FAPbI_3$-based LEDs[8,9].

The X-ray diffraction (XRD) measurements reveal the black γ-$CsSnI_3$ structure of all the films (Fig. 2c). The intensities of the characteristic peaks at 14.4° and 29.1° in N-S-$CsSnI_3$ show significant improvement compared with those of C- and S-$CsSnI_3$, indicating improved crystallinity (Supplementary Fig. 10)[39]. We identify the interaction mechanism between NPTU and $CsSnI_3$ using ^1H and ^{13}C nuclear magnetic resonance (NMR) spectroscopy. The resonance signal of $\delta = 181.42$ ppm arising from the C=S group in NPTU undergoes a chemical shift of $\Delta\delta \approx 0.24$ to $\delta = 181.18$ ppm and $\Delta\delta \approx 0.29$ to $\delta = 181.13$ ppm

https://doi.org/10.1038/s41566-023-01351-5

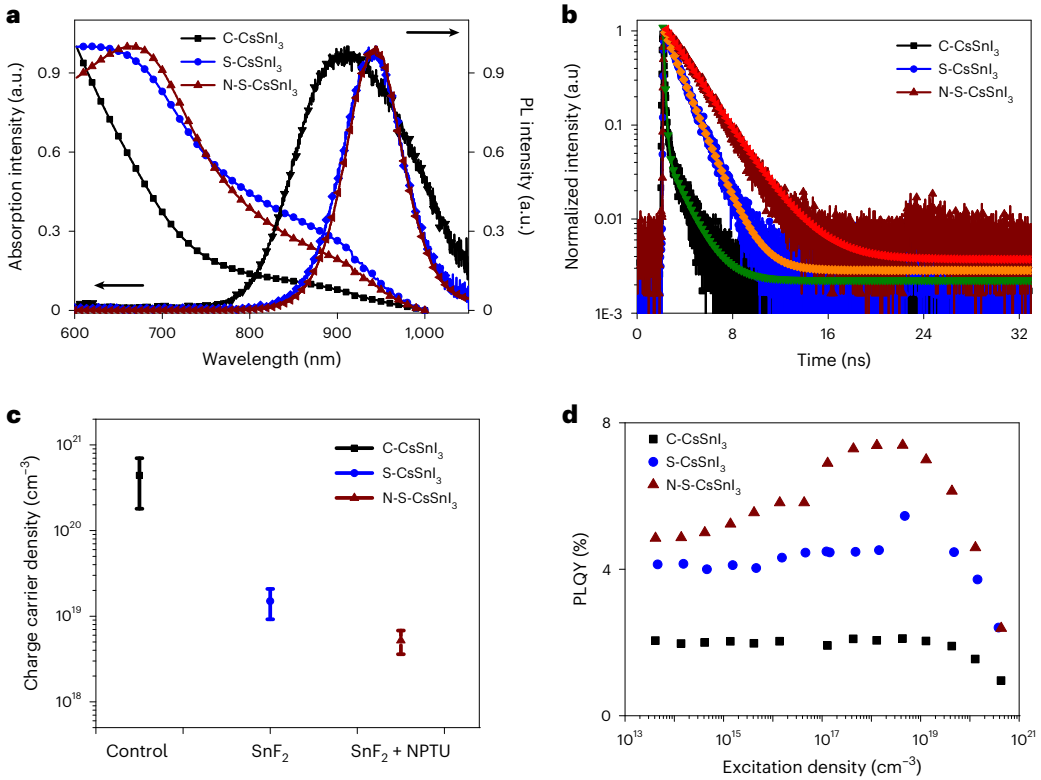

Fig. 3 | Optical and photophysical properties of $CsSnI_3$ films. a,**b**, Absorption and PL spectra (**a**) and time-resolved PL spectra and corresponding fitting spectra (**b**) of $CsSnI_3$ films. **c**, Charge carrier densities of $CsSnI_3$ films determined by Hall effect measurements. The error bars correspond to standard errors in the results calculated from the Hall effect measurement. **d**, Excitation-density-dependent PLQY of $CsSnI_3$ films. It should be noted that for the PLQY measurement, the $CsSnI_3$ films are covered with a thick PMMA layer, and then encapsulated with glass assisted by an ultraviolet curing adhesive. As such, the measured PLQY is external PLQY, rather than internal PLQY.

after interacting with the SnI_2 and CsI + SnI_2 mixture, respectively (Fig. 2d). Such variations indicate the occurrence of chemical interactions between the C=S group and SnI_2. In contrast, a smaller chemical shift of $\Delta\delta \approx 0.12$ ppm of the C=S group is observed after the addition of CsI. This comparison indicates that the interaction between NPTU and SnI_2 is much stronger than that between NPTU and CsI, ascribed to the stronger Lewis acid–base interaction between Sn^{2+} and NPTU compared with the relatively weak hydrogen bonding between the N–H group and I^-. The stronger interaction between NPTU and SnI_2 has also been confirmed by the ^{1}H NMR and attenuated total reflectance Fourier transform infrared spectroscopy data (Supplementary Figs. 11–14)[40,41].

The X-ray photoelectron spectra (XPS) further reveal the surface composition of $CsSnI_3$ and confirm their chemical interactions with NPTU. The S2*p* XPS peak of N-S-$CsSnI_3$ slightly shifts towards a higher binding energy compared with that of pure NPTU, indicating the lower electronegativity of S in N-S-$CsSnI_3$ (Supplementary Figs. 15–17). The proportion of Sn^{4+} was fairly high with the peak intensity comparable to that of Sn^{2+} in C-$CsSnI_3$ (Fig. 2e and Supplementary Fig. 17), suggesting the serious oxidation at the perovskite surface and grain boundaries. The easy oxidation of Sn^{2+} into Sn^{4+} is usually considered as the major source of trap-state formation in THPs. The Sn^{4+} content of N-S-$CsSnI_3$ is significantly reduced compared with C- and S-$CsSnI_3$. These results indicate that NPTU could prevent undesired tin oxidation due to the strong Lewis acid–base interaction of N–C=S···Sn^{2+}, which can increase the electron density around Sn^{2+}, offering excellent protection from being oxidized.

Controlled p doping and reduced trap density

Detailed optical and photophysical characterizations have revealed that NPTU/SnF_2 could control the p-doping density and reduce the trap density of $CsSnI_3$. C-$CsSnI_3$ shows a broad absorption band with an onset at ~1,000 nm and a broadband photoluminescence (PL) emission peak at ~915 nm with a large FWHM of more than 150 nm (Fig. 3a). In contrast, S- and N-S-$CsSnI_3$ show an ~30 nm redshifted emission peak centred at ~945 nm with reduced FWHM values of 82 and 74 nm, respectively. The time-resolved PL spectra of N-S-$CsSnI_3$ show distinct monoexponential decay and increased carrier lifetime of 2.28 ns compared with that of 0.49 and 1.37 ns for C- and S-$CsSnI_3$, respectively (Fig. 3b and Supplementary Table 1)[42–45]. The blueshift and broadening of the PL spectra as well as the short carrier lifetime of C-$CsSnI_3$ are indicative of a large concentration of hole charge carrier accumulation near the valence band maximum due to the strong self p doping, which can be explained based on a dynamic Burstein–Moss shift (Supplementary Fig. 18). The Hall effect measurements indicate significantly reduced p-doping density of $CsSnI_3$ after the incorporation of SnF_2 and NPTU (Fig. 3c and Supplementary Fig. 19), qualitatively agreeing with the results from ultraviolet photoelectron spectroscopy measurements (Supplementary Fig. 20).

The carrier recombination dynamics in THPs can be described by using a kinetic model that simulates the generation and recombination of charge carriers in the presence of both p doping and deep carrier traps (Supplementary Fig. 21). Through a qualitative analysis of the influence of p doping and trap carrier densities on the carrier recombination dynamics, we can learn how they affect the measurable figures of merit such as the internal photoluminescence quantum yield (PLQY) and the carrier lifetime (τ) (ref. 38). By simulating the excitation-density-dependent internal PLQY with hole-doping densities from 10^{14} to 10^{20} cm^{-3} and trap densities from 10^{15} to 10^{18} cm^{-3} (Supplementary Figs. 22–24), we learn that (1) the trap and hole-doping densities play a competing role in determining the carrier recombination dynamics and optical properties of $CsSnI_3$; (2) the presence of free

https://doi.org/10.1038/s41566-023-01351-5

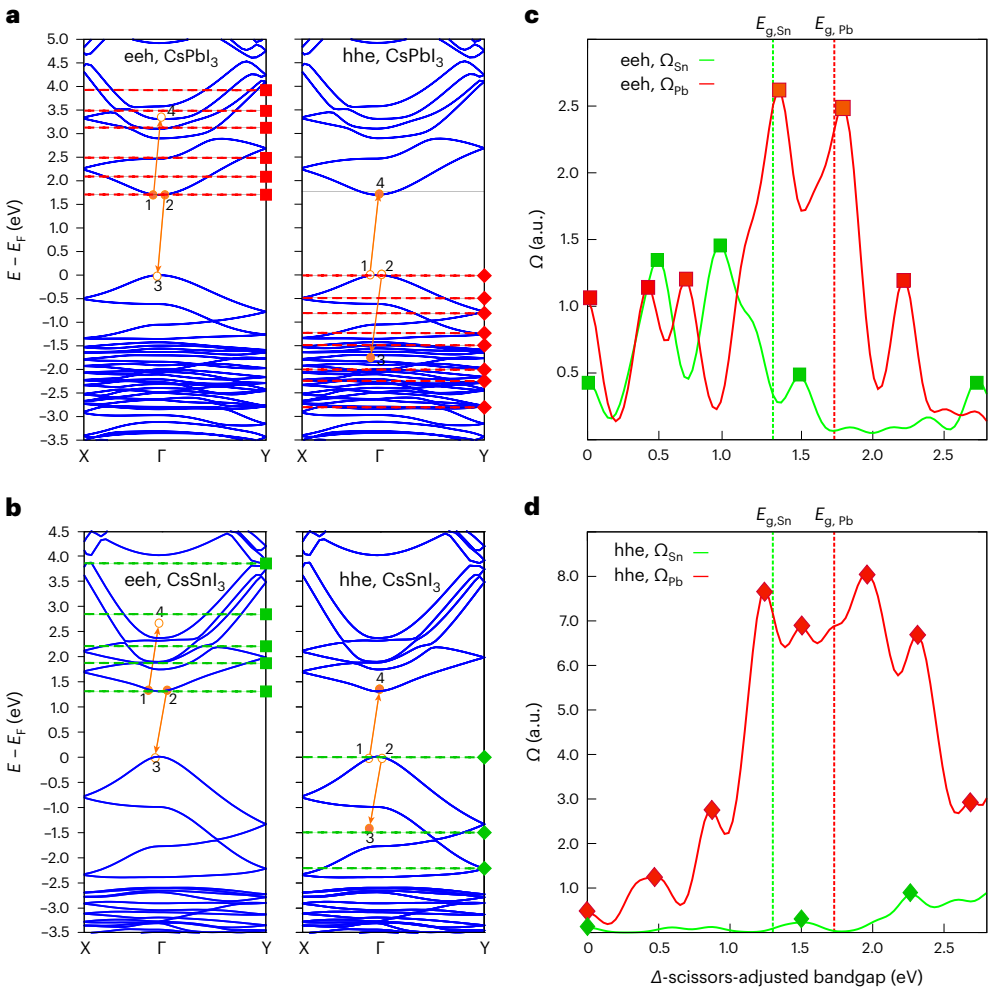

Fig. 4 | Auger recombination processes. a,**b**, Dispersions near the band extrema of $CsPbI_3$ (**a**) and $CsSnI_3$ (**b**) following the path X–Γ–Y. The representative transitions involved in the eeh or hhe mechanisms are depicted within both **a** and **b** using unidirectional arrows. **c**,**d**, Calculated available phase space for the direct Auger recombination process for $CsSnI_3$ and $CsPbI_3$ via the eeh (**c**) and hhe (**d**) mechanisms as a function of Δ-scissors-adjusted gap. The dashed vertical lines in **c** and **d** represent the experimental bandgaps of $CsSnI_3$ (green) and $CsPbI_3$ (red) and are marked by $E_{g,Sn}$ and $E_{g,Pb}$, respectively. The horizontal dashed red ($CsPbI_3$) and green ($CsSnI_3$) lines in **a** and **b** indicate the value of Δ-scissors-adjusted gap (eV) with respect to the conduction band minima (eeh) or valence band maxima (hhe) for which the peaks in the respective spectra of Ω are observed. For the range of Δ-scissors-adjusted bandgap in **c** and **d**, Ω{hhe} is nearly four orders of magnitude larger than Ω{eeh}.

background holes due to p doping may improve the PLQY and boost the radiative recombination with photogenerated electrons—this is true for increasing doping densities until Auger recombination becomes dominant; and (3) when the trap density is comparable to or higher than the doping density, trap-mediated recombination processes dominate and mostly influence the PLQY.

The excitation-density-dependent PLQY values of $CsSnI_3$ films are recorded and interpreted with the support of the abovementioned kinetic model. C-$CsSnI_3$ shows a constant, low PLQY in a wide range of excitation densities (Fig. 3d), which could be ascribed to the severe Auger recombinations due to the high hole-doping density of more than 10^{20} cm^{-3}. On the contrary, S- and N-S-$CsSnI_3$ show improved PLQY in the whole excitation-density range with gradually reduced hole-doping density, which is visible in the emergence of trap-filling processes at low excitation densities that are completely hidden by Auger recombinations in C-$CsSnI_3$. By comparing S- and N-S-$CsSnI_3$, the trap density is reduced after the incorporation of NPTU, as revealed by the shift in the trap-filling-induced PLQY increase towards a lower-excitation-density region, as well as temperature-dependent PL (Supplementary Figs. 25–27), femtosecond transient absorption (fs-TA) spectra (Supplementary Figs. 28–34).

Electronic structure calculations

Considering the possible influence of the hole-doping density on the Auger recombination process, we perform electronic structure calculations to understand the mechanism behind the Auger recombination in $CsSnI_3$. With the aim of highlighting the differences in THP and its well-known lead counterpart, we lay out the relation between the Auger recombination rate and phase-space volume for Auger processes (Ω). The electronic structure calculations of black γ-$CsSnI_3$ and $CsPbI_3$ reveal that the value of Ω for $CsSnI_3$ should be much lower compared with $CsPbI_3$, and consequently, owing to similarities between the two compounds, the recombination rates should follow the same trend. Figure 4a,b maps the peaks in Ω to energy levels in the band structures of $CsPbI_3$ and $CsSnI_3$. The arrows illustrate the typical eeh and hhe mechanisms, with the empty and filled circles representing holes and electrons, respectively. These eigenstates marked by numbers 1, 2, 3 and 4 correspond to the convention used in equation (1). We note that within a reasonable proximity to the band extrema, the number of available eigenstates, interpreted as points on the energy bands, are significantly larger in the case of a lead-based perovskite compared with its tin-based counterpart, leading to a large phase-space volume for $CsPbI_3$. At the same time, the peaks in the spectrum of Ω (Fig. 4c,d) match fairly well

with the density of available eigenstates for the three-body process in the band structure (Fig. 4a,b). These results imply that $CsSnI_3$ probably has a much lower Auger recombination rate than $CsPbI_3$. The calculated much smaller phase-space volume indicates that the high hole-doping density in $CsSnI_3$ could be beneficial for its light emission properties. In particular, it has been previously suggested that the rate of Auger recombination in cubic $CsSnI_3$ should be lower than that in cubic $CsPbI_3$, owing to features in the band structure that are also quantified here via a calculation of Ω (ref. 46).

$$\Omega = \sum_{1234} f_1 f_2 (1-f_3)(1-f_4)\delta(\varepsilon_1 + \varepsilon_2 - \varepsilon_3 - \varepsilon_4) \quad (1)$$

Discussions

Based on the discussions above, we can conclude that $CsSnI_3$ probably shows an intrinsically much lower Auger recombination rate than $CsPbI_3$, indicating that the intrinsic p-doping characteristic of $CsSnI_3$ could lead to improved PLQY due to the radiative recombination of background holes with the photogenerated electrons. The combination of these features provides rich opportunities for fabricating high-performance NIR LEDs that can operate at high current densities. As such, the record radiance and low efficiency roll-off of $CsSnI_3$ NIR LEDs could be ascribed to the capability of withstanding high current densities above 2,800 mA cm^{-2} due to the low Auger recombination rate, the elaborately controlled p doping and reduced trap densities realized via the NPTU/SnF_2 incorporation strategy.

The improved device stability can be ascribed to different concomitant phenomena. First, we have demonstrated an intrinsic lower Auger recombination rate for $CsSnI_3$ with respect to $CsPbI_3$. In addition, the possibility of controlling the p-doping concentration allows us to be in such a condition where the carrier density generated at 100 mA cm^{-2} is relatively small, with respect to the free hole density, and the latter is small enough to boost the radiative band-to-band recombination instead of fully entering the Auger recombination regime. Second, the energy barrier for ion migration is much larger in THP than that of its lead-based counterparts[47]. It is important to notice that in lead-based perovskites, photoinstability has been attributed to the trapping of carriers at halide interstitial deep defects, which eventually leads to the formation of I_2 molecules and promotes halide migration. However, this does not apply to THPs, as its defect chemistry is primarily determined by Sn, resulting in remarkable photostability even under high excitation densities[47]. The degradation of the device may be attributed to the damage occurring at the interface between the transport layer and emission layer.

Conclusion

In summary, we have demonstrated highly bright and stable long-wavelength NIR LEDs based on all-inorganic lead-free $CsSnI_3$. A facile yet effective strategy is developed to elaborately control the intrinsic p-doping density and reduce the trap density by retarding the crystallization process of $CsSnI_3$. The long-wavelength NIR LEDs based on $CsSnI_3$ not only demonstrate high radiance but also exhibit excellent stability, which is more than one order of magnitude longer than that of the best-known long-wavelength NIR LEDs fabricated with other kinds of soft material. Our work addresses the critical challenges of the low radiance and poor operational stability of long-wavelength NIR LEDs, representing a key step towards their practical applications. Moreover, the strategy to control the p-doping and trap densities can be extended to the design of other highly emissive and stable THP for light-emitting applications, including electrically pumped lasers.

Online content

Any methods, additional references, Nature Portfolio reporting summaries, source data, extended data, supplementary information, acknowledgements, peer review information; details of author contributions and competing interests; and statements of data and code availability are available at https://doi.org/10.1038/s41566-023-01351-5.

References

1. Medintz, I. L., Uyeda, H. T., Goldman, E. R. & Mattoussi, H. Quantum dot bioconjugates for imaging, labelling and sensing. *Nat. Mater.* **4**, 435–446 (2005).
2. Konstantatos, G. et al. Ultrasensitive solution-cast quantum dot photodetectors. *Nature* **442**, 180–183 (2006).
3. Kim, S. et al. Near-infrared fluorescent type II quantum dots for sentinel lymph node mapping. *Nat. Biotechnol.* **22**, 93–97 (2004).
4. Sun, L. et al. Bright infrared quantum-dot light-emitting diodes through inter-dot spacing control. *Nat. Nanotechnol.* **7**, 369–373 (2012).
5. Yoon, J. et al. GaAs photovoltaics and optoelectronics using releasable multilayer epitaxial assemblies. *Nature* **465**, 329–333 (2010).
6. Walther, T., Cullis, A., Norris, D. & Hopkinson, M. Nature of the Stranski-Krastanow transition during epitaxy of InGaAs on GaAs. *Phys. Rev. Lett.* **86**, 2381 (2001).
7. Tuong, Ly,K. et al. Near-infrared organic light-emitting diodes with very high external quantum efficiency and radiance. *Nat. Photon.* **11**, 63–68 (2017).
8. Cao, Y. et al. Perovskite light-emitting diodes based on spontaneously formed submicrometre-scale structures. *Nature* **562**, 249–253 (2018).
9. Xu, W. et al. Rational molecular passivation for high-performance perovskite light-emitting diodes. *Nat. Photon.* **13**, 418–424 (2019).
10. Wei, Y. C. et al. Overcoming the energy gap law in near-infrared OLEDs by exciton-vibration decoupling. *Nat. Photon.* **14**, 570–577 (2020).
11. Gong, X. et al. Highly efficient quantum dot near-infrared light-emitting diodes. *Nat. Photon.* **10**, 253–257 (2016).
12. Pradhan, S. et al. High-efficiency colloidal quantum dot infrared light-emitting diodes via engineering at the supra-nanocrystalline level. *Nat. Nanotechnol.* **14**, 72–79 (2019).
13. Gao, L. et al. Efficient near-infrared light-emitting diodes based on quantum dots in layered perovskite. *Nat. Photon.* **14**, 227–233 (2020).
14. Vasilopoulou, M. et al. Efficient colloidal quantum dot light-emitting diodes operating in the second near-infrared biological window. *Nat. Photon.* **14**, 50–56 (2020).
15. Dong, Y. et al. Bipolar-shell resurfacing for blue leds based on strongly confined perovskite quantum dots. *Nat. Nanotechnol.* **15**, 668–674 (2020).
16. Wang, Y.-K. et al. All-inorganic quantum-dot LEDs based on a phase-stabilized α-$CsPbI_3$ perovskite. *Angew. Chem. Int. Ed.* **60**, 16164–16170 (2020).
17. Wang, Y.-K. et al. Chelating-agent-assisted control of $CsPbBr_3$ quantum well growth enables stable blue perovskite emitters. *Nat. Commun.* **11**, 3674 (2020).
18. Zheng, X. et al. Chlorine vacancy passivation in mixed halide perovskite quantum dots by organic pseudohalides enables efficient Rec. 2020 blue light-emitting diodes. *ACS Energy Lett.* **5**, 793–798 (2020).
19. Wang, Z. et al. Multifunctional p-type carbon quantum dots: a novel hole injection layer for high-performance perovskite light-emitting diodes with significantly enhanced stability. *Adv. Opt. Mater.* **7**, 1901299 (2019).
20. Qiu, W. et al. Mixed lead–tin halide perovskites for efficient and wavelength-tunable near-infrared light-emitting diodes. *Adv. Mater.* **31**, 1806105 (2019).
21. Yu, H. Q. et al. Alkalis-doping of mixed tin-lead perovskites for efficient near-infrared light-emitting diodes. *Sci. Bull.* **67**, 54–60 (2022).

22. Lu, J. X. et al. Dendritic $CsSnI_3$ for efficient and flexible near-infrared perovskite light-emitting diodes. *Adv. Mater.* **33**, 2104414 (2021).
23. Yuan, F. et al. Color-pure red light-emitting diodes based on two-dimensional lead-free perovskites. *Sci. Adv.* **6**, eabb0253 (2020).
24. Wang, K. et al. Lead-free organic-perovskite hybrid quantum wells for highly stable light-emitting diodes. *ACS Nano* **15**, 6316–6325 (2021).
25. Liang, H. et al. High color purity lead-free perovskite light-emitting diodes via Sn stabilization. *Adv. Sci.* **7**, 1903213 (2020).
26. Lin, R. et al. Monolithic all-perovskite tandem solar cells with 24.8% efficiency exploiting comproportionation to suppress Sn(II) oxidation in precursor ink. *Nat. Energy.* **4**, 864–873 (2019).
27. Lin, J. et al. Harnessing dielectric confinement on tin perovskites to achieve emission quantum yield up to 21%. *J. Am. Chem. Soc.* **141**, 10324–10330 (2019).
28. Yakunin, S. et al. High-resolution remote thermometry and thermography using luminescent low-dimensional tin-halide perovskites. *Nat. Mater.* **18**, 846–852 (2019).
29. Hong, W. et al. Efficient low-temperature solution-processed lead-free perovskite infrared light-emitting diodes. *Adv. Mater.* **28**, 8029–8036 (2016).
30. Xue, S. et al. Advances in electrically driven light-emitting diodes based on lead-free metal halides. *Chem. Commun.* **59**, 1116–1124 (2023).
31. Wei, Q. et al. Chances and challenges for tin perovskites. *Trends Chem.* **4**, 1–4 (2022).
32. Chung, I. et al. $CsSnI_3$: semiconductor or metal? High electrical conductivity and strong near-infrared photoluminescence from a single material. High hole mobility and phase-transitions. *J. Am. Chem. Soc.* **134**, 8579–8587 (2012).
33. Ricciarelli, D. et al. Instability of tin iodide perovskites: bulk p-doping versus surface tin oxidation. *ACS Energy Lett.* **5**, 2787–2795 (2020).
34. Li, B. et al. Tin-based defects and passivation strategies in tin-related perovskite solar cells. *ACS Energy Lett.* **5**, 3752–3772 (2020).
35. Barrigón, E. et al. Synthesis and applications of III–V nanowires. *Chem. Rev.* **119**, 9170–9220 (2019).
36. Tsintzos, S. et al. A GaAs polariton light-emitting diode operating near room temperature. *Nature* **453**, 372–375 (2008).
37. Feldmann, S. et al. Photodoping through local charge carrier accumulation in alloyed hybrid perovskites for highly efficient luminescence. *Nat. Photon.* **14**, 123–128 (2020).
38. Treglia, A. et al. Effect of electronic doping and traps on carrier dynamics in tin halide perovskites. *Mater. Horiz.* **9**, 1763–1773 (2022).
39. Zhang, X. et al. First-principles simulation of carrier recombination mechanisms in halide perovskites. *Adv. Eng. Mater.* **10**, 1902830 (2020).
40. Meng, X. et al. Crystallization kinetics modulation of $FASnI_3$ films with pre-nucleation clusters for efficient lead-free perovskite solar cells. *Angew. Chem. Int. Ed.* **60**, 3693–3698 (2021).
41. Wang, S. et al. High-performance perovskite solar cells with large grain-size obtained by using the Lewis acid-base adduct of thiourea. *Sol. RRL* **2**, 1800034 (2018).
42. Guo, Q. et al. Passivation of the grain boundaries of $CH_3NH_3PbI_3$ using carbon quantum dots for highly efficient perovskite solar cells with excellent environmental stability. *Nanoscale* **11**, 115–124 (2019).
43. Ye, T. et al. Ambient-air-stable lead-free $CsSnI_3$ solar cells with greater than 7.5% efficiency. *J. Am. Chem. Soc.* **143**, 4319–4328 (2021).
44. Milot, R. et al. The effects of doping density and temperature on the optoelectronic properties of formamidinium tin triiodide thin films. *Adv. Mater.* **30**, 1804506 (2018).
45. Bubnova, O. et al. Semi-metallic polymers. *Nat. Mater.* **13**, 190–194 (2014).
46. Shen, J. et al. Unexpectedly strong Auger recombination in halide perovskites. *Adv. Energy Mater.* **8**, 1801027 (2018).
47. Martani, S. et al. Defect engineering to achieve photostable wide bandgap metal halide perovskites. *ACS Energy Lett.* **8**, 2801–2808 (2023).

Methods

Materials

Chemicals listed below are commercially available and used without further purification. Tin(II) iodide (SnI_2, 99.999%), tin(II) fluoride (SnF_2, 99.000%), caesium iodide (CsI, 99.999%) and NPTU (>98.000%) were purchased from Sigma-Aldrich. PEDOT:PSS (AI 4083) was purchased from Ossila. All the other materials used for the device fabrication were purchased from Sigma-Aldrich.

Electronic structure calculations

The electronic structure calculations of black γ-$CsSnI_3$ and $CsPbI_3$ were performed using the Vienna ab initio simulation package using the projector augmented wave method. The PBEsol functional in the framework of density functional theory was used for geometry optimization, whereas the hybrid HSE functional with 50% exact Hartree–Fock exchange for short-range interactions and a screening parameter of $\omega = 0.20$ $Bohr^{-1}$ was implemented to evaluate the band structure. We use 50% exact Hartree–Fock exchange as that provides the best conformity between the HSE and GW band structures, the latter requiring a very high computational cost for a dense sampling of the Brillouin zone, which is essential to calculate meaningful values of Ω. To fully account for relativistic effects, the spin–orbit interaction was included in all the calculations.

Preparation of perovskite solution and films

The control precursor solution without additives (denoted as C-$CsSnI_3$) was prepared by dissolving 112 mg SnI_2 and 73 mg CsI in 1 ml DMSO (0.3 M: the concentration was determined by the Sn content). The precursor solution with SnF_2 (denoted as S-$CsSnI_3$) was prepared by dissolving 112.0 mg SnI_2, 73.0 mg CsI and 4.7 mg SnF_2 in 1 ml DMSO (0.3 M, 10% SnF_2). The NPTU solution was prepared by dissolving 152 mg of NPTU in 1 ml DMSO (1 M). As for the NPTU-added precursor solution, a certain amount of NPTU (1 M) was added in the S-$CsSnI_3$ precursor solution to achieve the desired composition (denoted as N-S-$CsSnI_3$). The solution was stirred and filtered before spin coating. Emissive layers of $CsSnI_3$ with different compositions were spin coated in a nitrogen-filled glovebox (concentrations of H_2O and O_2, <0.1 ppm) via a two-step process, 1,000 r.p.m. for 10 s (acceleration speed, 200 r.p.m. s^{-1}) and then 5,000 r.p.m. for 60 s (acceleration speed, 800 r.p.m. s^{-1}), followed by annealing at 100 °C for 10 min to form the active emission layer. The optimized doping content for NPTU is 40% (mole fraction compared with Sn). For the PL, low-temperature-dependent PL, time-resolved PL, ultraviolet–visible absorption spectra, fs-TA spectra and XRD measurements, 80 mg ml^{-1} polymethyl methacrylate (PMMA)/chlorobenzene solution was spin coated at 6,000 r.p.m. for 50 s on top of the perovskite layer.

Optical characterization

The ultraviolet–visible absorption spectra were measured using a PerkinElmer model LAMBDA 900a. Steady-state PL spectral measurements were performed on an Andor Shamrock 303i spectrograph equipped with an Andor Newton electron-multiplying charge-coupled device instrument (DU970N-UVB). During the measurement, the charge-coupled device detector was cooled to −45 °C. The sample was excited by a Thorlabs collimated laser-diode-pumped DPSS laser module (CPS532), and a 550 nm long-pass filter was used to protect the detector. The wavelength of the system was calibrated by a mercury lamp. The intensity of the spectra was calibrated by a standard halogen lamp (AvaLight-HAL-S-Mini) from Avantes. A laser (405 nm, 75 ps pulse width) was used as the excitation source at 10 MHz repetition rate (Edinburgh Instruments) for the time-resolved PL spectra measurement. The laser was focused onto the sample by an air objective (numerical aperture, 0.7; spot size, ~1 μm; Mitutoyo). The PL data of the sample were collected by the same objective and sent to an avalanche photodiode (timing resolution, ~40 ps; ID Quantique) in a time-correlated single-photon counting system (timing jitter, ~3 ps; qutools) with an instrument response function of ~56 ps. Fluence-dependent PLQY values were acquired by focusing the second harmonic of an Yb:KGW laser (Light Conversion Pharos, 515 nm, 30 fs pulse duration, 1 kHz repetition rate) on thin films of $CsSnI_3$ within a fluence range between 4.0×10^{13} and 2.5×10^{20} cm^{-3}, and collecting the emitted PL on a fibre spectrometer (Ocean Optics Maya Pro 2000). Relative PLQY measurements were calibrated by scaling the resulting PLQY curve to an absolute PLQY measurement conducted in an integrating sphere (Labsphere). For the PLQY measurement, the $CsSnI_3$ films were covered with a thick PMMA layer, and then encapsulated with glass assisted by an ultraviolet curing adhesive.

Low-temperature-dependent PL spectra

The samples were mounted in a closed-cycle cryostat (DE-202AE) from Advanced Research Systems. The cooling was performed by a helium compressor (ARS-4HW) from the same company. The temperature control was performed by a Lake Shore 330 autotuning temperature controller. During the measurement, the cryostat was kept in a vacuum. The PL excitation and detection were performed by an objective, a 45°-angled 552 nm long-pass dichroism glass and optical fibres. The laser light was coupled into a fibre, out of a collimator, then reflected by the glass and finally focused by the objective into the cryostat. The emission from the sample passed the cryostat window, the objective, the glass, a collimator, a fibre, a collimator again and finally focused into the spectrograph.

fs-TA measurement

The fs-TA spectroscopy was conducted with a HELIOS fs-TA spectrometer (Ultrafast Systems). A portion of the 800 nm fundamental output from the regenerative amplifier (Coherent Libra, 1 kHz, 50 fs) was used to pump an optical parametric amplifier (Coherent OPerA Solo). The 650 nm pump pulses were generated from an optical parametric amplifier. Another portion of the 800 nm fundamental beam was focused into a 10 mm sapphire crystal to generate a broadband NIR continuum (800–1,600 nm) that was used as the probe pulse. The probe beam was passed through an 850 nm long-pass filter to eliminate the residual 800 nm fundamental components to prevent strong secondary photoexcitation of the sample. The signals were collected using a complementary metal–oxide–semiconductor sensor within the spectrometer.

Hall measurements

The Hall measurements were performed in a chip with van der Pauw geometry. The four bottom contact electrodes were deposited with Cr and Au. The $CsSnI_3$ films were encapsulated with PMMA to avoid degradation. The chips were placed perpendicular to the magnetic field changing from −1.2 to 1.2 T. The applied current and voltage were recorded by Keithley 2400 and Nanovoltmeter model 2182A instruments, respectively. All the measurements were performed in air at room temperature.

Structural, morphological and chemical characterizations

The XRD measurements were conducted using an X-ray diffractometer (PANalytical X'Pert Pro) with an X-ray tube (Cu Kα, $\lambda = 1.5406$ Å). The attenuated total reflectance Fourier transform infrared measurements were performed on a PIKE MIRacle attenuated total reflectance accessory with a diamond prism in a Vertex 70 spectrometer (Bruker) using a DLATGS detector at room temperature. The spectra were acquired at a 2 cm^{-1} resolution. SEM was conducted using a Philips XL30 FEG SEM instrument under a voltage of 8 kV. Proton (^1H) NMR (500 MHz) and carbon (^{13}C) NMR (126 MHz) were recorded on a Varian 500 MHz spectrometer at room temperature. Dried DMSO-d_6 was used as the solvent and to calibrate the NMR isotropic chemical shifts. XPS (monochromatized Al Kα, $h\nu = 1{,}486.6$ eV) spectra were recorded with a Scienta 200 hemispherical analyser and calibrated

by referencing to the Fermi level and Au4*f*7/2 peak position of the Ar^+-ion sputter-clean gold foil.

Device fabrication and characterization

ITO-coated glass substrates were cleaned by sonication in deionized water and then in organic solvents (acetone followed by ethanol), and then dried under a nitrogen flow. The substrates were cleaned using an ultraviolet–plasma treatment to enrich the ITO surface with oxygen and increase the ITO work function. The PEDOT:PSS hole injection layer was spin coated at 4,000 r.p.m. (acceleration speed, 4,000 r.p.m. s^{-1}) for 40 s on ITO followed by annealing in air at 150 °C for 30 min, and then $CsSnI_3$ films were deposited on PEDOT:PSS in a nitrogen-filled glovebox. Finally, the substrates were transferred to a vacuum chamber, where TPBi (55 nm) and LiF/Al electrodes (1/150 nm) were deposited using a thermal evaporation system through a shadow mask under a high vacuum of 1×10^{-6} torr. The device active area was 7.25 mm^2 as defined by the overlapping area of the ITO and Al electrodes. The performance of the LEDs was measured in a nitrogen-filled glovebox at room temperature. A Keithley 2400 source meter and a fibre integration sphere (FOIS-1) coupled with a QE Pro spectrometer (Ocean Optics) were used for the LED measurements. It should be noted that our LED setup was programmed to measure the EL spectra ranging from 350 to 930 nm. Therefore, the full-range EL spectra up to 1,100 nm were then obtained from another spectrometer (Shamrock 303i; the detector is an Andor Newton electron-multiplying charge-coupled device) with a wide emission detection range driven by a Keithley 2400 source meter, and the performance is, thus, calibrated by the comparison of the EL spectra measured in the LED setup and from Shamrock 303i. The LED stability was measured either in the glovebox in a small confined space (without a nitrogen flow) or in a home-made nitrogen-filled box at room temperature with nitrogen flow, as specified in the figures. The devices were driven by a Keithley 2400 source meter at a constant current and the light emission signals were measured using a commercial photodiode.

Data availability

The data that support the findings of this study are available from the corresponding author upon reasonable request.

Acknowledgements

We thank B. Guan and L. Liang from the Institute of Chemistry, Chinese Academy of Sciences, for the cross-sectional SEM measurement; H. Zhang for help with the EL, PL and low-temperature-dependent PL spectra measurements; Z. Hu and J. Zhang for the NMR spectra measurement; C. Wang for the XPS and ultraviolet photoelectron spectroscopy measurements; H. Lei for the SEM characterization; C. Kuang for the Fourier transform infrared spectra measurement; and L. Sui for help with the carrier recombination dynamic simulations. F.Y. acknowledges financial support from the National Key Research and Development Program of China (2023YFB3611800), National Natural Science Foundation of China (22302012), National Science Fund for Excellent Young Scholars (Overseas) and Special Funds for Introducing Talents from Beijing Normal University (312200502508). F.G. acknowledges support from Knut and Alice Wallenberg Foundation (Dnr. KAW 2019.0082), the European Research Council Consolidator Grant (LEAP, 101045098), the Swedish Research Council Vetenskapsrådet (grant 2020-03564) and the Swedish Government Strategic Research Area in Materials Science on Functional Materials at Linköping University (faculty grant SFO-Mat-LiU no. 2009-00971). I.A.A. is a Wallenberg Academy Scholar (grant no. KAW-2018.0194). S.I.S. acknowledges support from the Swedish Research Council (VR) (project no. 2019-05551) and the ERC (synergy grant FASTCORR project 854843). T.C.S. and J.W.M.L. acknowledge support from the Singapore Ministry of Education under its MOE Tier 2 grant (MOE-T2EP50120-0004) and the National Research Foundation (NRF) Singapore under its NRF Investigatorship (NRF-NRFI2018-04). A.P., G.F. and A.T. acknowledge funding from the European Union's Horizon 2020 research and innovation programme through the ERC project SOPHY under grant agreement no. 771528, the MSCA-ITN SMART-X under grant agreement no. 860553 and the Marie Skłodowska-Curie grant agreement no. 956270. The computations were enabled by resources provided by the National Academic Infrastructure for Supercomputing in Sweden (NAISS) and the Swedish National Infrastructure for Computing (SNIC) at the National Supercomputer Center (NSC) and Center for High Performance Computing (PDC), partially funded by the Swedish Research Council through grant agreement nos. 2022-06725 and 2018-05973.

Author contributions

F.G. and F.Y. conceived the idea and designed the experiments. F.Y. prepared the samples and carried out the device fabrication and measurements. F.Y., G.F., A.T. and A.P. conducted the carrier recombination dynamic simulations and PLQY measurement. T.L. helped with the device stability and Hall effect measurement. J.W.M.L. and T.C.S. performed the fs-TA measurements. U.S., J.K., S.I.S. and I.A.A. conducted the theoretical calculations. F.Y. wrote the first draft of the paper. All authors discussed the results and contributed to the paper.

Funding

Open access funding provided by Linköping University.

Competing interests

F.Y. and F.G. are filing a patent application related to this work.

Additional information

Supplementary information The online version contains supplementary material available at https://doi.org/10.1038/s41566-023-01351-5.

Correspondence and requests for materials should be addressed to Feng Gao.

Peer review information *Nature Photonics* thanks the anonymous reviewers for their contribution to the peer review of this work.